PbI_2 nanocrystal growth by atomic layer deposition of $Pb(tmhd)_2$ and HI

Jacob N. Vagott[1], Kathryn Bairley[1], Juanita Hidalgo[1], Carlo A.R. Perini[1], Andrés-Felipe Castro-Méndez[1], Sarah Lombardo[1], Barry Lai[2] Josh Kacher[1], Juan-Pablo Correa-Baena[1*]

[1]School of Materials Science and Engineering, Georgia Institute of Technology, North Ave NW, Atlanta, Georgia 30332, USA

[2]Advanced Photon Source, Argonne National Lab, 9700 S. Cass Avenue, Lemont, IL 60439 USA

Corresponding author: JPCB jpcorrea@gatech.edu

ORCID:

Juan-Pablo Correa-Baena 0000-0002-3860-1149

Jacob N. Vagott 0000-0003-3057-7209

Juanita Hidalgo 0000-0002-5832-3262

Carlo A.R. Perini 0000-0001-7582-2234

Andrés-Felipe Castro-Méndez 0000-0001-8320-353X

Abstract

Atomic layer deposition (ALD) allows for a great level of control over the thickness and stoichiometry of materials. ALD provides a suitable route to deposit lead halides, which can further be converted to perovskite for photovoltaics, photoemission, and photodetection, among other applications. Deposition of lead halides by ALD has already begun to be explored; however, the precursors used in published processes are highly hazardous, require expensive fabrication processes, or contain impurities that can jeopardize the optoelectronic properties of metal halide perovskites after conversion. We sought to deposit lead iodide (PbI_2) by a facile ALD process involving only two readily accessible, low-cost precursors and without involving any unwanted impurities that could act as recombination centers once the PbI_2 is later converted to perovskite. Crystalline PbI_2 nanocrystals were grown on soda-lime glass (SLG), silicon dioxide support grids, and silicon wafer substrates and provide the groundwork for further investigation into developing

lead halide perovskite processes by ALD. The ALD-grown PbI_2 was characterized by annular dark field scanning transmission electron microscopy (ADF-STEM), atomic force microscopy (AFM), and x-ray photoemission spectroscopy (XPS), among other methods. This work presents the first step to synthesize lead halide perovskites with atomic control for applications such as interfacial layers in photovoltaics and for deposition in microcavities for lasing.

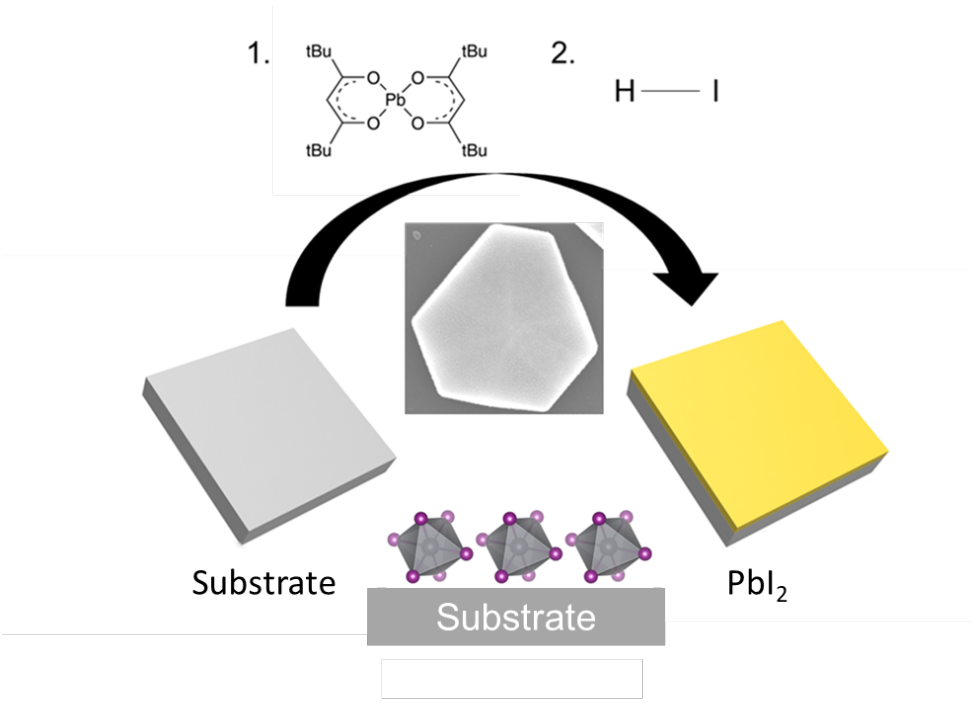

Introduction

Several deposition methods exist for PbI_2. Namely, chemical vapor deposition (CVD) and thermal evaporation are the most utilized vapor deposition routes, while spin-coating is the most applied solution deposition method. Thermally evaporated PbI_2 has previously been used for applications including x-ray detection [1], photoemission [2], and photovoltaics [3], [4]. However, thermal evaporation requires temperatures approaching 400°C in order to vaporize the PbI_2 powder and lacks the atomic-level thickness control that is enabled by atomic layer deposition (ALD)

processes. CVD of PbI_2 encounters similar limitations, requiring higher substrate temperatures than ALD and typically resulting in thicker films with poor control over thickness [5], [6].

ALD is a vapor deposition technique that allows for a great level of control over process parameters including thickness, conformity, and stoichiometry [7]–[9]. As a vapor deposition process, ALD can deposit uniform films over large areas, making it ideal for different optoelectronic applications. For example, lead halide perovskites are a relatively new class of materials that have been used with great success for optoelectronic applications including perovskite solar cells (PSCs), LEDs, and photodetection, such as x-ray and γ-ray detection [10]–[12]. In lead halide perovskites, ALD has been used to deposit some electron transport layers, for example, SnO_2 [13], [14]. Given the advantages of ALD for ultra-thin film deposition, this technique could also be tuned, engineered, and designed to deposit the photoactive material itself, the lead halide perovskite. As a starting point, lead iodide, a precursor of lead iodide perovskites, was deposited through ALD as an initial step for the fine-tune engineering of ultra-thin lead halide perovskites.

ALD processes are self-limiting in nature, can be fine-tuned to result in ultrathin films of any required thickness, and are compatible with high throughput roll-to-roll (R2R) manufacturing [15]–[17]. ALD holds advantages over thermal evaporation in that it has finer thickness control and utilizes self-limiting reactions. Lead halide perovskites are of particular interest to deposit by ALD to improve the morphology, crystallization, uniformity and for deposition of ultra-thin films. Lead halide perovskites are typically deposited by spin-coating, a type of solution processing that is restricted to small-area substrates and lacks reliability, conformality, and uniformity. Vapor deposition methods such as thermal evaporation and ALD can solve many of these problems. Lead halide perovskites can be obtained by a two-step process, where a lead halide is first deposited and

further reacted with an organic halide to form a perovskite film. This process has been used to improve the morphology of the perovskite layer obtained by spin-coating [18] and thermal evaporation [19], [20]. Moreover, ALD could be used to have a thinner layer with less defects and more homogeneity. When considering $MAPbI_3$, which is the most studied lead halide perovskite, the lead halide precursor of interest is PbI_2. The possibility of depositing $MAPbI_3$ single crystals by ALD is of particular interest, since the presence of grain boundaries results in a much larger number of defects, more hysteresis behavior, and result in lower-performing devices [21]–[23]. However, since MAPbI3 has not been deposited by ALD, lead halide deposition through ALD is a first step.

ALD has only recently been considered as a means of depositing PbI_2. The first study to do so, conducted in 2014 by Sutherland et. al., fabricated a PbS film by ALD and converted the layer to PbI_2 outside of the reactor through exposure to iodine gas [24]. Popov et. al. went a step further in 2019 by fabricating PbI_2 by sequentially reacting lead (II) bis[bis(trimethylsilyl)amide] ($Pb(btsa)_2$) with SnI_4 [25]. While promising, this deposition process leaves tin impurities in the resultant PbI_2 film, which leads to the formation of deep traps once the layer is converted into perovskite, preventing its use for many optoelectronic applications, including photovoltaics and photodetection. Moreover, $Pb(btsa)_2$ is not commercially available.

In this work, we deposited PbI_2 free of recombination-active impurities with a simple, one-step ALD process using readily available precursors for lead and iodine. We conducted X-ray photoelectron spectroscopy (XPS) and grazing incidence wide angle X-ray scattering (GIWAXS) measurements, which confirmed that we deposited crystalline PbI_2. To gain a better understanding of the morphology of PbI_2, we used scanning electron microscopy (SEM), annular dark-field scanning transmission electron microscopy (ADF-STEM), and atomic force microscopy (AFM).

We investigated the growth with increasing number of cycles, where we observed a decreasing growth rate but less impurities in the resultant PbI_2. Through this novel PbI_2 process, we were able to deposit PbI_2 nanocrystals with fine thickness control. Fine control over lead iodide deposition through ALD is a fundamental step in the path of designing and controlling the deposition of ultra-thin lead halide perovskite films.

Results and Discussion

Film Deposition

The choice of PbI_2 precursors is essential to produce perovskite films with good optoelectronic properties, as well as to limit fabrication costs. As such, we screened different ALD precursors for the deposition of the PbI_2 layer for low-cost, high reactivity and vapor pressure, and commercial availability. Several lead precursors were considered as the lead source, with bis(2,2,6,6-tetramethyl-3,5-heptanedionato) lead (II) ($Pb(tmhd)_2$), lead (II) acetylacetonate ($Pb(acac)_2$), and bis(1-dimethylamino-2-methyl-2-propanolate) lead (II) ($Pb(dmamp)_2$) being the most notable. $Pb(tmhd)_2$ has been used before for ALD of PbO_x, showing reasonable volatility when heated to its melting point (127°C) and above [26]. $Pb(acac)_2$ has also been used successfully as an ALD and metal organic chemical vapor deposition (MOCVD) precursor, although it has lower volatility due primarily to increased shielding of the cationic lead center [27]. $Pb(dmamp)_2$ has the highest vapor pressure among them, and is reasonably reactive, but is over ten times more expensive when compared to $Pb(tmhd)_2$. For these reasons, $Pb(tmhd)_2$ was chosen as the lead precursor. Hydroiodic acid (HI) was chosen as co-reactant to provide the iodine, given its commercial availability as well as high volatility and low cost. HI was chosen over alternative iodine precursors such as TiI_4 and SnI_4 as it does not include any unwanted metals that may contribute to recombination sites once the PbI_2 is converted to perovskite. It was considered that using aqueous

HI may introduce PbO impurities into the deposited PbI_2, although HI was found to react much more vigorously, disallowing any PbO from being formed. However, careful handling/storage of HI must be observed due to its high acidity, volatility, and corrosiveness.

Deposition of PbI_2 was primarily conducted on glass and silicon wafer substrates, where the surface is terminated largely by hydroxyl groups. Reaction of the substrate surface with the $Pb(tmhd)_2$ proceeds by ligand-exchange reaction as such:

$$Si - OH + Pb(tmhd)_2 \rightarrow Si - O - Pb - tmhd\_ + H - tmhd \quad (1)$$

While this reaction is ideal, steric hinderance due to the relatively large tmhd ligands will result in space between each chemisorbed Pb atom, disallowing a full monolayer to be formed[28]. In addition, the surface is unlikely to be completely covered by hydroxyl groups, leading to Pb atoms being dispersed along the substrate surface. Upon dosing of HI, a second ligand-exchange reaction takes place:

$$Si - O - Pb - tmhd + 2HI \rightarrow Si - O - PbI_2 + 2(H - tmhd) \quad (2)$$

After a number of ALD cycles, the PbI_2 is able to rearrange as governed by its lattice parameters. Surface diffusion of the PbI_2 is also likely to occur to some extent, leading to the formation of PbI_2 nanocrystals. At lower temperatures, the PbI_2 is more likely to form a polycrystalline film rather than nanocrystals due to the effective pinning of the Pb atoms at low temperatures[29], [30]. To examine this behavior, a broad temperature range (60°C -150°C) was considered; however, growth only occurred between 75°C and 120°C. In this study, 120°C was primarily used as the substrate temperature; however, lower temperatures were also investigated. While it is expected that at low temperatures the tmhd ligand may be difficult to fully purge away, further studies detailing post-annealing methods to remove impurities may be useful in further development of low temperature (<120°C) processes.

Details of the ALD process can be found in Figure S1. Dose times of 1.5s and 0.5s were used for $Pb(tmhd)_2$ and HI, respectively. A purge time of 20s was used between each precursor pulse in order to allow for excess precursors to be evacuated from the chamber. For HI, being that the temperature in the chamber is relatively low for an ALD process (<200°C), four smaller doses were used as opposed to one large dose to aid in purging and to help ensure a complete reaction [31]. When the temperature was raised to 150°C, deposition only took place on the edges of the underside of the substrates, which suggests that a lower temperature is needed for ALD growth. This behavior was also reported in high-temperature trials by Popov et. al [25].

Crystal structure and orientation

To determine the crystal structure of the deposited PbI_2 thin layer, grazing incidence wide-angle x-ray scattering (GIWAXS) measurements were taken on the as-deposited 81 and 162 cycles of PbI_2. Given the better coverage of PbI_2 on SLG, these measurements were also done to the tin layers deposited on SLG. The diffraction circular average (Figure 1a) shows the comparison between peak intensities for 81 cycles versus 162 cycles. We observed that the peaks in the diffraction pattern match the peaks of PbI_2 found in literature values [32], [33]. The 001 peak was the most prominent, which is typical [34]. Given that the 001 peak was the highest in intensity, the crystals were preferentially oriented to the 001 plane. Further, other PbI_2 Bragg peaks were scattered which matched the simulated peaks for PbI_2 as it is seen in blue in Figure 1a. However, an additional peak at around q_r ~2 was observed for the 81 cycles deposition that did not correspond to crystalline PbI_2, giving an insight that there was a crystalline impurity for this deposition condition. The impurity peak was not present for the 162 cycles deposition condition.

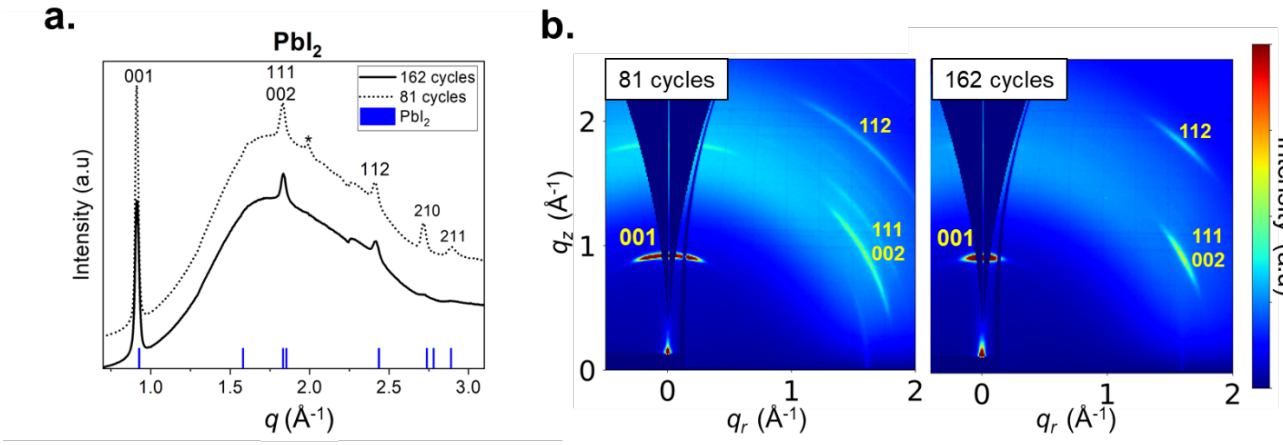

Figure 1. GIWAXS data for PbI_2 deposited at 120°C on SLG including **A)** Circular average plots for 81 and 162 cycles and 2D GIWAXS for **B)** 81 cycles and **C)** 162 cycles.

Further, to get additional information about preferential orientation, we looked at the 2D GIWAXS images in Figure 1b. For the 162-cycle deposition, the smaller peaks fade and the PbI_2 nanocrystals show less diffraction signal for 001 when compared to the 81-cycle deposition, which may help result in greater ease-of-reaction with MAI [35], [36].

Chemical composition

X-ray photoelectron spectroscopy (XPS) was used to analyze the chemical composition at the surface of deposited PbI_2 nanocrystals. Figure S2 shows the survey spectra for 81 and 162 cycles of PbI_2 deposited at 120°C on SLG, and the individual spectra for Pb4f and I3d are shown in Figure 2a. C1s and O1s spectra are shown in Figure S2b. From the survey spectra, we can clearly see the presence of lead and iodine as well as peaks from the silicon oxide of the substrate. This is due to the incomplete coverage of the substrate by the PbI_2 nanocrystals.

To confirm the chemical composition of the surface of the deposited PbI_2 nanocrystals, XPS spectra for Pb4f and I3d were analyzed. There was no shift in peaks found between 81 and 162 cycles. Peaks for Si2s and O1s were present and corresponded to the typical peaks for silicon substrates with an O1s peak at 532.0 eV and Si2s peak at 103.2 eV. The Pb4f peak (Figure 2a)

agrees well with the accepted binding energy for the $Pb4f_{7/2}$ peak at 138.6 eV [37]. Similarly, the $I3d_{5/2}$ peak at 619.5 eV is identical to previously reported literature values for $I3d_{5/2}$ in PbI_2 [38]. The ratio of I:Pb at the surface was found to be 2.7 for 81 cycles and 2.4 for 162 cycles, suggesting that there is a more ideal stoichiometry achieved after 162 cycles. We hypothesize that the excess of iodine at the surface is due to the presence of hydrogen bonding of HI onto the surface of the PbI_2 nanocrystals.

Notably, peaks associated with PbO_x are not present. PbO_x could be found in the deposited PbI_2 if either the tmhd ligand is not completely purged from the chamber or if $Pb(tmhd)_2$ reacts with the water found in aqueous HI. This suggests that 120°C is hot enough to encourage dissociation of the tmhd ligand and that the water in the HI is not a cause for concern at this temperature.

To further analyze the chemical composition in the bulk of the deposited PbI_2 thin films, we measured synchrotron X-ray Fluorescence (XRF) to observe the elemental mapping of a 30x30 μm^2 area of the film. XRF signals for Pb and I were quantified into mass values and then converted into moles in order to calculate and observe the stoichiometry of the bulk of the material deposited. In PbI_2, the expected molar ratio is 2. Therefore, we calculated the molar ratio between iodide and lead (I:Pb) and mapped it as observed in Figure 2b for both deposition conditions. First, we observed a difference in homogeneity between 81 cycles and 162. For 81 cycles, more iodine-rich (bright yellow) regions were observed – which are heterogeneous – whereas for the 162 cycles the overall film was more homogeneous. Both deposition conditions showed some regions of a molar ratio of 1 (black), which indicated that the PbI_2 thin film did not form a layer of complete coverage over the SLG surface. Moreover, we also observed the elemental mapping of the molar ratio I:Pb on silicon wafer substrates, showing more heterogeneity. Overall, 162 cycles showed better

coverage and homogeneity of the PbI_2 with a molar ratio around 2 as expected, and the ALD deposition over SLG was more homogeneous and had a better coverage than on silicon wafer. It can be confirmed that PbI_2 is being deposited by the GIWAXS peaks (Figure 1), and this is further corroborated by the surface composition from XPS and the XRF maps (Figure 2).

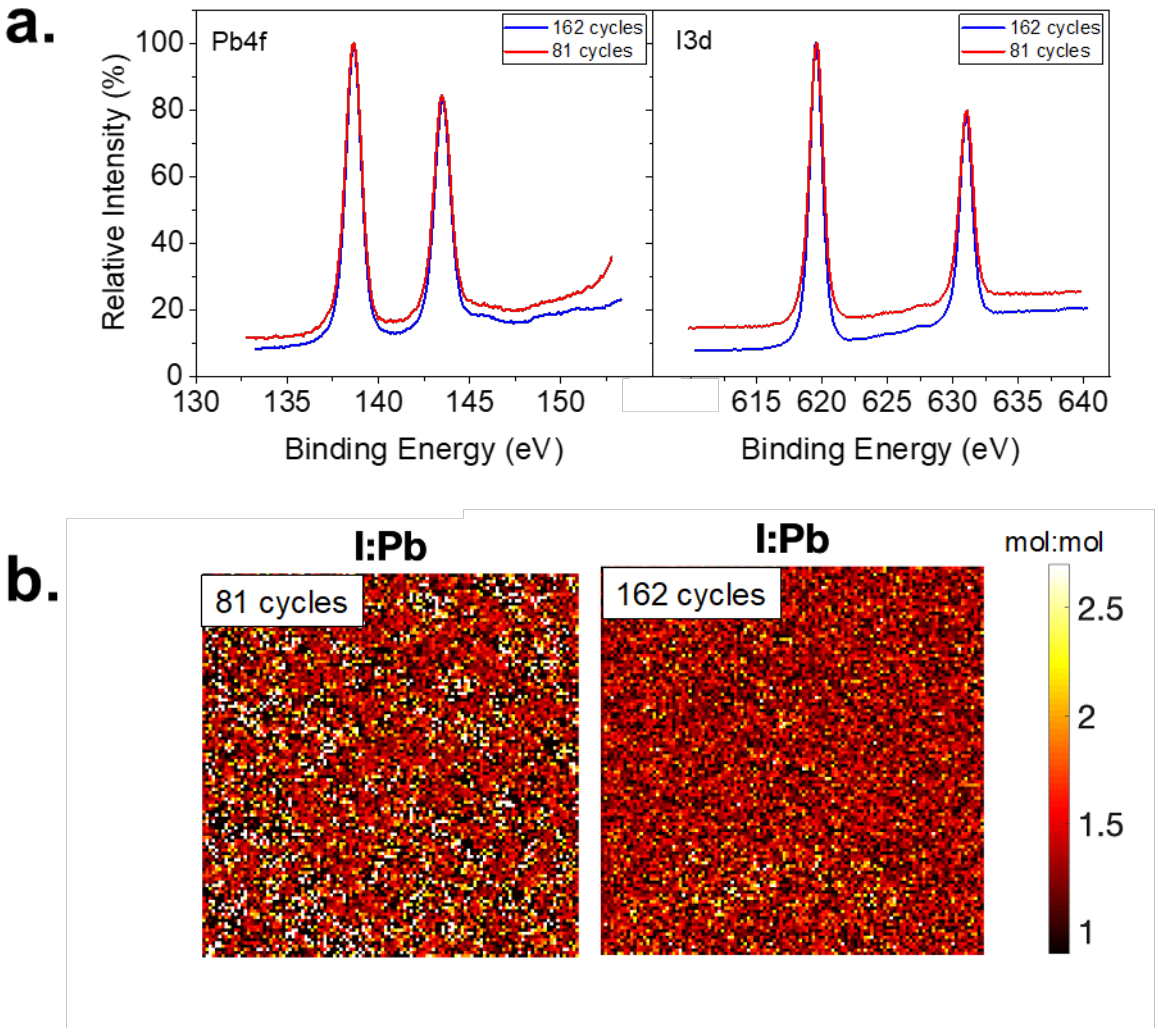

Figure 2. A) elemental Pb4f and I3d XPS spectra for 81 and 162 cycles of PbI_2 deposited on SLG at 120°C. **B)** XRF mapping of the elemental molar ratio I: Pb for 81 and 162 cycles deposited on SLG (30x30 μm^2).

Morphology of PbI_2 films

The films deposited had a light-yellow appearance as it is seen in the pictures shown in Figure 3a,b. Visually, the layer deposited with 162 cycles looked slightly darker, suggesting the possible formation of a thicker film. In order to investigate the morphology of the ALD films deposited, we used SEM (Figure 3c,d). The SEM images of films deposited on silicon wafers can be found in Figure S3. As seen in Figure 3c,d, the resultant PbI_2 is made up of clearly-defined PbI_2 nanocrystal clusters as opposed to a uniform thin film. As observed in the XRF mapping in Figure 2b, the PbI_2 was not uniformly deposited. While typically considered unideal for ALD processes, this behavior has been seen before in ALD of nanoparticles and nanocrystals [29], [30]. Surface-limited nucleation sites are the likely cause of the nanocrystals growing independently, where both steric hinderance from $Pb(tmhd)_2$ association as well as the lack of complete hydroxyl group coverage on the substrate result in island formation [29], [39]. Figure 3c shows hexagonal nanocrystals of PbI_2 after 81 cycles of the PbI_2 process. The hexagonal shape is consistent with the expected crystal structure for PbI_2 and in agreement with previous literature reports [25], [40]. After 162 cycles, the crystals have grown in diameter while maintaining a hexagonal shape (Figure 3d). The same trend can be observed for the crystals deposited on a silicon wafer (Figure S3). SEM revealed crystal sizes in the range of 200—500 nm (diameter) for 81 cycles, with an average value of approximately 375 nm. For 162 cycles, the diameter increased to a range of 600—1050 nm and an average of 850 nm. This increase may be attributed to coalescence of smaller nanocrystals over the course of the ALD deposition process. However, the hexagonal crystal shape is present in all depositions in the present study as well as in [40]–[43].

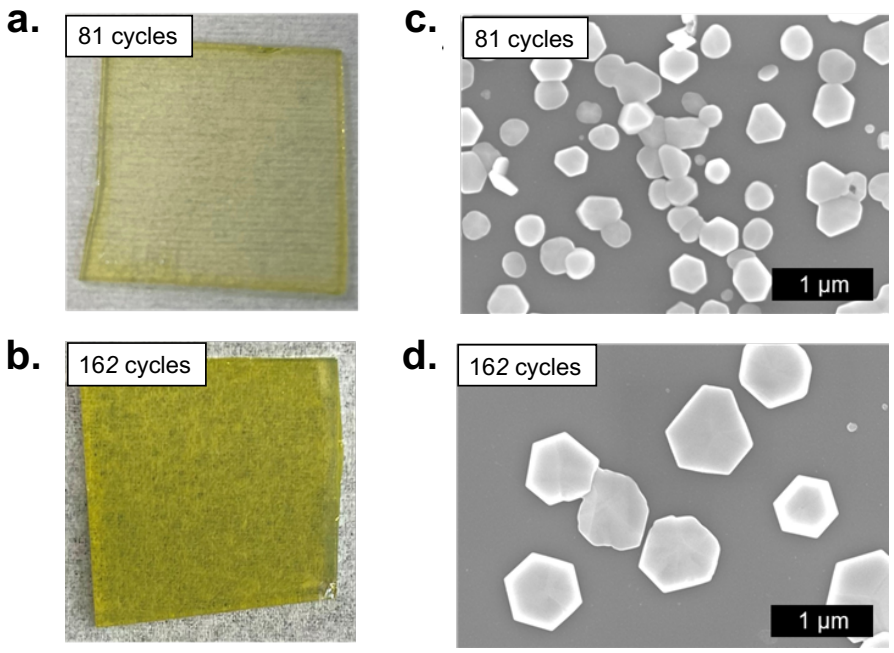

Figure 3. Optical and SEM images for ALD PbI_2 deposited at 120°C on approximately 1x1 inch SLG substrates. **A)-B)** optical images of 81 and 162 cycles, respectively. **C)-D)** SEM images of 81 and 162 cycles

To better distinguish the PbI_2 crystals and surface morphology, ADF-STEM images were taken of the as-deposited PbI_2 on silicon dioxide support grids at 120°C. In Figure 4a,b, the planar hexagonal crystals can be clearly distinguished. Figure S4 shows additional images taken by the TEM. PbI_2 crystals of diameter primarily between 200-400 nm are observed, which agrees well with the diameters from SEM images of 81 cycles of PbI_2. For the 162 cycles of PbI_2, STEM images show more interconnected crystals of similar size, which contrasts with the larger, less connected crystals seen in SEM after the same deposition conditions. This is presumably due to the difference in the concentration of hydroxyl groups on the surface of the substrate between the SLG and silicon dioxide support grid. Atomic resolution images were achieved (Figure 4c,f), which allowed for the calculation of d-spacing values. The primary method to determine the d-spacing was to perform a Fast Fourier Transform (FFT) on a crystalline region of the deposited

material (Figure 4g) and measure the peak spacings in the diffractogram. The FFT shows a double hexagon pattern, which matches well the FFT reported by Alberti et. al. for 2H-PbI_2, and the corresponding d-spacings of 3.81 Å for the outer hexagon and 2.15 Å for the inner hexagon match well with previously report values [43]. Along with the fact that the 2H phase is the most stable PbI_2 configuration at room temperature, this leads us to conclude that the PbI_2 crystals deposited by our ALD process are predominantly of the 2H phase. The 3.81 Å spots would not be present in the electron diffraction pattern for 6H-PbI_2 [43].

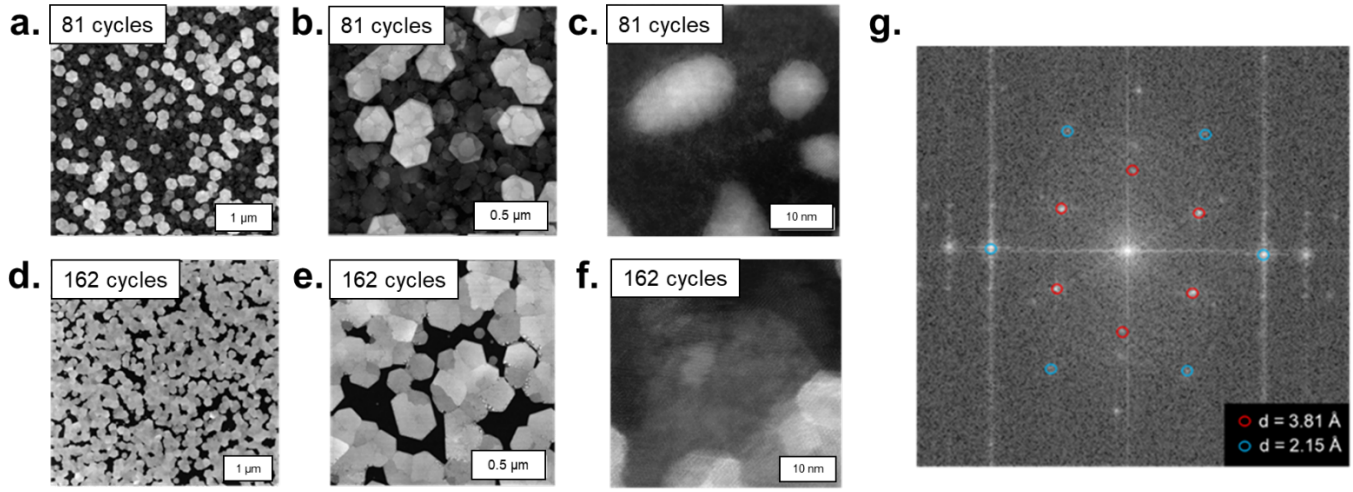

Figure 4. ADF-STEM images of PbI_2 grown on silicon oxide support grids after **A)-C)** 81 ALD cycles and **D)-F)** 162 ALD cycles of PbI_2, and **G)** Fast-Fourier Transform (FFT) for a PbI_2 nanocrystal (162 cycles).

To investigate the topology and thickness of the PbI_2 thin films, AFM measurements were performed on the PbI_2 deposited on silicon wafer. Height plots (Figure 5c,d) and phase plots (Figure 5a,b) were produced for comparison of the PbI_2 deposited at 120°C. From the AFM images gathered for 81 cycles of PbI_2, the average crystal thickness was found to be 51 nm, although the

largest crystal was ~90 nm. This scales relatively linearly with the average crystal thickness being 87 nm for 162 cycles of PbI_2 deposited at 120°C. The amplitude error plots and z-sensor plots also taken by AFM can be found in Figure S5.

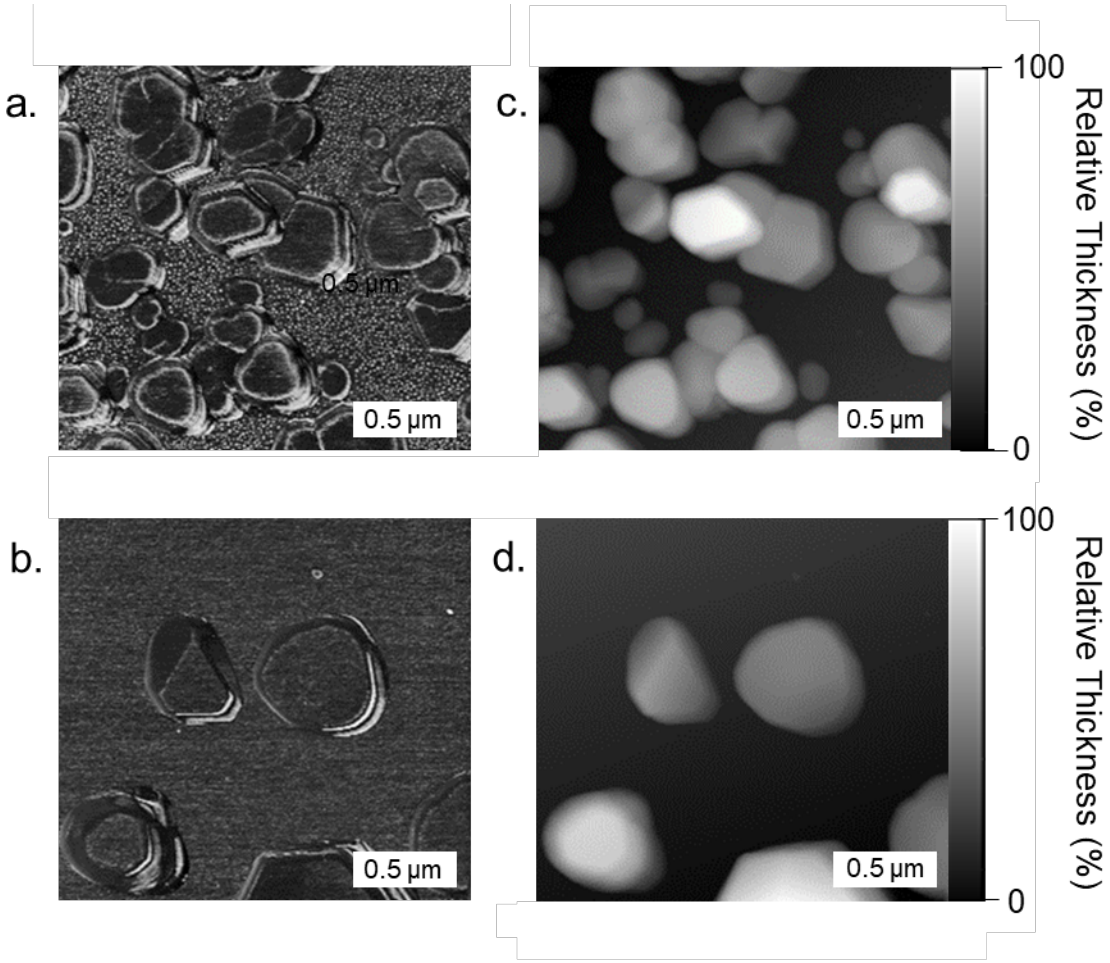

Figure 5. AFM images for PbI_2 deposited on silicon wafers at 120°C. **A)-B)** phase images for 81 and 162 cycles, respectively and **C)-D)** height images for 81 and 162 cycles, respectively.

Perhaps the most important aspect of an atomic layer deposition processes is its self-limiting nature. To investigate whether or not the PbI_2 was growing linearly, the average thickness of the nanocrystals was determined by AFM after various numbers of cycles (Figure 6a,b). While the growth per cycle (GPC) decreases with increasing number of cycles, there is a strong linear trend. The decrease in GPC that is observed is likely due to the decreasing number of nucleation

sites on the substrate, which are more favorable than nucleation on existing nanocrystals. Similar to the increasing thickness, there is also an observed linear trend in the increasing diameter of the nanocrystals with increasing number of cycles. After 500 cycles, nanocrystals above 1 micron in diameter were able to be achieved (Figure 6a). This allows for control over both the nanosheet thickness and diameter by manipulating the number of cycles in the ALD process.

In order to determine if the PbI_2 precursors are saturating the surface, the thicknesses of the nanocrystals were determined after various precursor dosing times (Figure 6c,d). From Figure 6c, since there is little change in sheet thickness, it can be said that HI is saturating somewhere between 0.1 and 0.5 seconds, while $Pb(tmhd)_2$ is saturating the surface with a dose time of 0.5 seconds (Figure 6d).

Given that there is linear trend in growth with increasing number of cycles, as well as the apparent saturation of both precursors, the PbI_2 growth appears to be self-limiting. The large GPC observed (mean value of 4.34Å/cycle after 500 cycles) is likely due to the coalescence of PbI_2 nanocrystals.

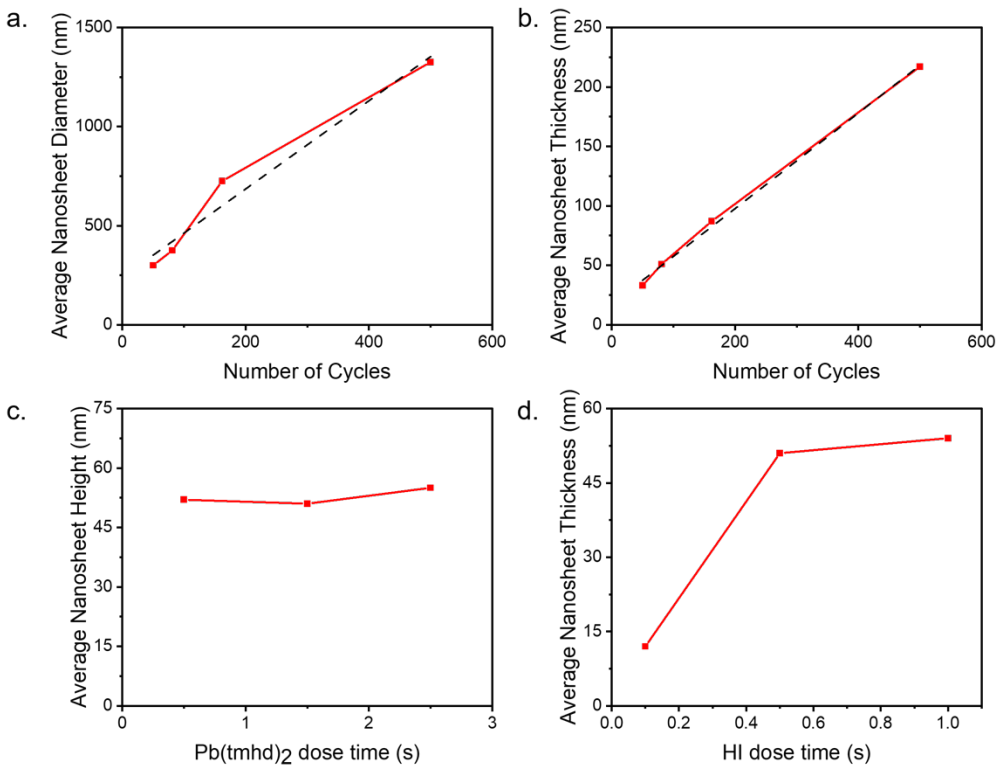

Figure 6. Saturation behavior analysis of PbI_2 grown by ALD on a silicon wafer at 120°C showing **A)** change in average nanosheet diameter of PbI_2 nanocrystals with number of cycles, **B)** change in average nanosheet thickness with number of cycles and change in average nanosheet thickness with dose time of **C)** $Pb(tmhd)_2$ and **D)** HI.

To investigate the effect of deposition temperature on the resulting PbI_2, a brief analysis of 100 cycles of PbI_2 deposited at 75, 90, and 120°C was performed. SEM and AFM images were obtained for each temperature in order to investigate the morphologies, and XPS was done to see how the I:Pb ratio and amount of impurities changes with temperature. We hypothesized that at lower temperatures (e.g. 75°C), we were more likely to have high coverage while also increasing the likelihood of impurities due to the ligand being more difficult to purge away at lower temperatures. As seen in Figure 7a,b, the coverage of the silicon substrate increases with decreasing temperature. At 90°C, the substrate is nearly covered, but there are some holes present

which can be seen in the AFM/SEM images as well as the Si2s spectra (Figure S8b). As expected, the Pb atoms appear to be pinned to the substrate at the lower temperatures, which allows for less diffusion and greater cohesion of the film [39].

The I:Pb ratio changes slightly across the temperature range, being 2.4, 2.6, and 2.7 for 75, 90, and 120°C, respectively. As expected, the Si-O peak at 532.0 eV is diminished for the films with greater coverage (75 and 90°C). The largest difference found through XPS analysis over this temperature range was in the O1s spectra. For both 75 and 90°C, there is a small peak at 529.5 eV, which is indictive of C=O bonds. These bonds likely come from the tmhd ligand, suggesting that the ligand is not completely purged from the surface at lower temperatures. The survey spectra as well as the C1s spectra for each temperature can be found in Figure S6a and Figure S6c, respectively. Since the I:Pb ratio is closer to stoichiometric, and the coverage is improved, further annealing studies must be conducted in the future to determine if the impurities from the ligand can be removed.

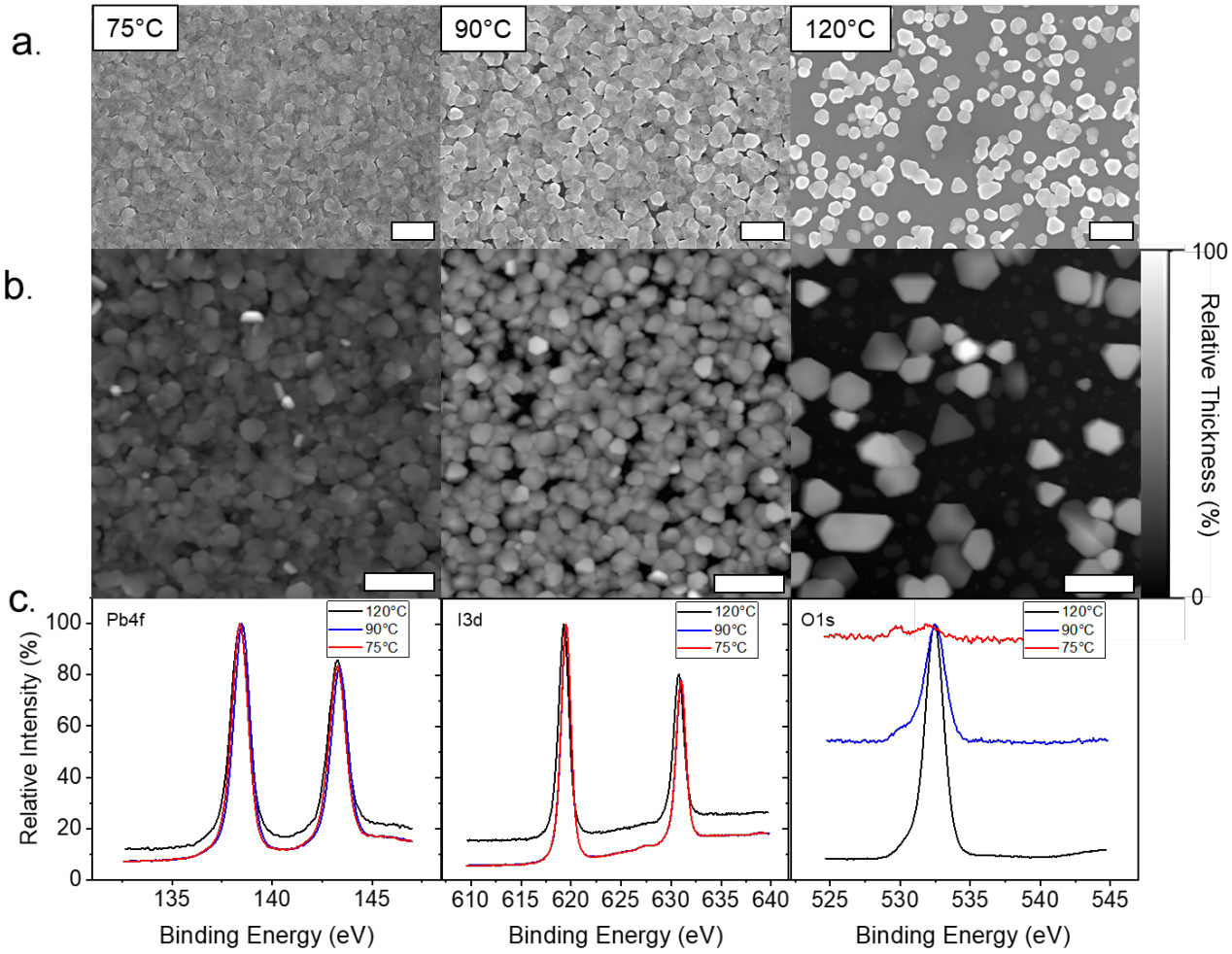

Figure 7. Temperature study of 100 cycles of PbI_2 deposited at 75, 90, and 120°C on silicon wafers including **A)** SEM images, **B)** AFM images, and **C)** XPS analysis.

Conclusions

We present a facile method of depositing PbI_2 using only commercially available precursors and a simple one-step ALD process. PbI_2 nanocrystals were deposited at 120°C and were determined to be of the 2H phase. Our process holds advantages over the lone past ALD process for PbI_2 by ALD in that the precursor used for iodine does not contain any unwanted metals such as tin, potentially making the PbI_2 more useful in areas such as photovoltaics, where the tin may decrease efficiency and lead to the formation of deep traps. This PbI_2 process may provide a route to depositing single-

crystalline $MAPbI_3$, which would remove the negative effects of grain boundaries on performance in various applications. In addition, we explored the effect of temperature on the surface characteristics and morphology of PbI_2 by ALD. While coverage and stoichiometric ratio are improved for low temperatures, further studies must be conducted to reduce impurities caused by leftover ligands in the film. PbI_2 by ALD is the first step towards depositing $MAPbI_3$ and other perovskites by a single ALD process and can be applied to fields including photovoltaics and photodetection, among others.

Experimental Section

Film Preparation

Primarily, SLG was used as the substrate, with <100>–oriented silicon wafers (University Wafer) and silicon dioxide support grids also being explored. The substrates were cleaned using a 2% Hellmanex III solution (Sigma Aldrich), DI water, acetone, and IPA. The films were first cleaned of surface impurities using the Hellmanex solution and sonicated for 10 minutes. The substrates were then rinsed with DI water before also being sonicated in DI water for 10 minutes. Afterwards, sequential sonication in acetone and IPA was conducted before the substrates were dried immediately and stored. Substrates were UV-Ozone cleaned for 15 minutes immediately prior to deposition in the ALD system. For TEM imaging, 8 nm silicon dioxide support films, 70x70 µm (Ted Pella, Inc.) were used as-is aside from 15 minutes of UV-Ozone cleaning directly prior to deposition.

$Pb(tmhd)_2$ (Strem Chemicals, Inc., 99%) was reacted with hydroiodic acid (57% in water, stabilized with hypophosphorous acid, 99.95%) to form PbI_2 films inside of a Kurt J. Lesker Company (KJLC) ALDLE150 reactor. Nitrogen was used as a carrier gas at a chamber pressure

of approximately 1 torr during deposition. The alternative lead precursor considered was $Pb(dmamp)_2$ (Strem Materials, Inc., 98%).

$Pb(tmhd)_2$ was stored in a stainless-steel bubbler from KJLC and heated to 145°C to provide ample vapor pressure. Hydroiodic acid was stored in a stainless-steel 50 mL cylinder from Strem Materials, Inc. and was held at room temperature with no direct temperature monitor. The ALD valves and lines for all precursors were held constant at 135°C with constant nitrogen flow as to avoid buildup of precursors in the system. The substrate and chamber temperature for all processes unless otherwise noted was 120°C, monitored at the substrate, upper chamber, and lower chamber levels. The dose time for the lead precursor was 1.5 seconds, with a purge time of 20 seconds. The hydroiodic acid was then dosed for 0.5 seconds and purged for 20 seconds. To increase reliability, one ALD cycle consisted of 1 dose $Pb(tmhd)_2$ and 4 doses of hydroiodic acid (Figure S1).

Morphology of PbI_2 thin films

Morphology of the PbI_2 films was investigated initially using an Hitachi SU8230 in the IEN/IMAT Materials Characterization Facility at Georgia Tech. TEM and HAADF images were taken using the Hitachi HT7700 TEM of the IEN/IMAT Materials Characterization Facility at Georgia Tech.

Acknowledgement:

This work was performed in part at the Georgia Tech Institute for Electronics and Nanotechnology, a member of the National Nanotechnology Coordinated Infrastructure (NNCI), which is supported by the National Science Foundation (Grant ECCS-1542174). J.V acknowledges the Georgia Tech Graduate Assistance in Areas of National Need (GAANN) fellowship for career funding.

References

[1] A. M. Caldeira Filho and M. Mulato, "Characterization of thermally evaporated lead iodide films aimed for the detection of X-rays," *Nucl. Instruments Methods Phys. Res. Sect. A Accel. Spectrometers, Detect. Assoc. Equip.*, vol. 636, no. 1, pp. 82–86, 2011, doi: 10.1016/j.nima.2011.01.093.

[2] C. Webb and P. M. Williams, "Angle resolved photoemission studies of the band structures of semiconductors: PbI2," *Surf. Sci.*, vol. 68, no. C, pp. 576–582, 1977, doi: 10.1016/0039-6028(77)90249-7.

[3] W. Soltanpoor *et al.*, "Hybrid Vapor-Solution Sequentially Deposited Mixed-Halide Perovskite Solar Cells," *ACS Appl. Energy Mater.*, vol. 3, no. 9, pp. 8257–8265, 2020, doi: 10.1021/acsaem.0c00686.

[4] J. Li *et al.*, "Highly Efficient Thermally Co-evaporated Perovskite Solar Cells and Mini-modules," *Joule*, vol. 4, no. 5, pp. 1035–1053, 2020, doi: 10.1016/j.joule.2020.03.005.

[5] S. Ngqoloda, C. J. Arendse, T. F. Muller, S. S. Magubane, and C. J. Oliphant, "Controlled deposition of lead iodide and lead chloride thin films by low-pressure chemical vapor deposition," *Coatings*, vol. 10, no. 12, pp. 1–13, 2020, doi: 10.3390/coatings10121208.

[6] Y. Wang *et al.*, "Chemical vapor deposition growth of single-crystalline cesium lead halide microplatelets and heterostructures for optoelectronic applications," *Nano Res.*, vol. 10, no. 4, pp. 1223–1233, 2017, doi: 10.1007/s12274-016-1317-1.

[7] R. W. Johnson, A. Hultqvist, and S. F. Bent, "A brief review of atomic layer deposition: From fundamentals to applications," *Mater. Today*, vol. 17, no. 5, pp. 236–246, 2014, doi: 10.1016/j.mattod.2014.04.026.

[8] M. A. Hossain *et al.*, "Atomic layer deposition enabling higher efficiency solar cells: A review," *Nano Mater. Sci.*, vol. 2, no. 3, pp. 204–226, 2020, doi: 10.1016/j.nanoms.2019.10.001.

[9] W. Li, Y. X. Xu, D. Wang, F. Chen, and Z. K. Chen, "Inorganic perovskite light emitting diodes with ZnO as the electron transport layer by direct atomic layer deposition," *Org. Electron.*, vol. 57, no. November 2017, pp. 60–67, 2018, doi: 10.1016/j.orgel.2018.02.032.

[10] A. K. Jena, A. Kulkarni, and T. Miyasaka, "Halide Perovskite Photovoltaics: Background, Status, and Future Prospects," *Chem. Rev.*, vol. 119, no. 5, pp. 3036–3103, 2019, doi: 10.1021/acs.chemrev.8b00539.

[11] H. Wei and J. Huang, "Halide lead perovskites for ionizing radiation detection," *Nat. Commun.*, vol. 10, no. 1, pp. 1–12, 2019, doi: 10.1038/s41467-019-08981-w.

[12] F. P. García De Arquer, A. Armin, P. Meredith, and E. H. Sargent, "Solution-processed semiconductors for next-generation photodetectors," *Nat. Rev. Mater.*, vol. 2, no. 3, 2017, doi: 10.1038/natrevmats.2016.100.

[13] S. Jeong, S. Seo, H. Park, and H. Shin, "Atomic layer deposition of a SnO2 electron-transporting layer for planar perovskite solar cells with a power conversion efficiency of 18.3%," *Chem. Commun.*, vol. 55, no. 17, pp. 2433–2436, 2019, doi: 10.1039/c8cc09557d.

[14] H. H. Park, "Inorganic materials by atomic layer deposition for perovskite solar cells," *Nanomaterials*, vol. 11, no. 1, pp. 1–21, 2021, doi: 10.3390/nano11010088.

[15] O. Lupan *et al.*, "Ultra-thin TiO2 films by atomic layer deposition and surface functionalization with Au nanodots for sensing applications," *Mater. Sci. Semicond.*

Process., vol. 87, no. July, pp. 44–53, 2018, doi: 10.1016/j.mssp.2018.06.031.

[16] V. Zardetto *et al.*, "Atomic layer deposition for perovskite solar cells: Research status, opportunities and challenges," *Sustain. Energy Fuels*, vol. 1, no. 1, pp. 30–55, 2017, doi: 10.1039/c6se00076b.

[17] R. T. Piper, T. B. Daunis, W. Xu, K. A. Schroder, and J. W. P. Hsu, "Photonic Curing of Nickel Oxide Transport Layer and Perovskite Active Layer for Flexible Perovskite Solar Cells: A Path Towards High-Throughput Manufacturing," *Front. Energy Res.*, vol. 9, no. March, pp. 1–12, 2021, doi: 10.3389/fenrg.2021.640960.

[18] D. Bi, A. M. El-Zohry, A. Hagfeldt, and G. Boschloo, "Improved morphology control using a modified two-step method for efficient perovskite solar cells," *ACS Appl. Mater. Interfaces*, vol. 6, no. 21, pp. 18751–18757, 2014, doi: 10.1021/am504320h.

[19] N.-G. Park and K. Zhu, "Scalable fabrication and coating methods for perovskite solar cells and solar modules," *Nat. Rev. Mater.*, vol. 5, no. 5, pp. 333–350, May 2020, doi: 10.1038/s41578-019-0176-2.

[20] R. Ji *et al.*, "Thermally evaporated methylammonium-free perovskite solar cells," *J. Mater. Chem. C*, vol. 8, no. 23, pp. 7725–7733, 2020, doi: 10.1039/d0tc01550d.

[21] J. W. Lee, S. H. Bae, N. De Marco, Y. T. Hsieh, Z. Dai, and Y. Yang, "The role of grain boundaries in perovskite solar cells," *Mater. Today Energy*, vol. 7, pp. 149–160, 2018, doi: 10.1016/j.mtener.2017.07.014.

[22] Z. Chu *et al.*, "Impact of grain boundaries on efficiency and stability of organic-inorganic trihalide perovskites," *Nat. Commun.*, vol. 8, no. 1, pp. 1–8, 2017, doi: 10.1038/s41467-017-02331-4.

[23] H. Mehdizadeh-Rad, F. Mehdizadeh-Rad, F. Zhu, and J. Singh, "Heat mitigation in

perovskite solar cells: The role of grain boundaries," *Sol. Energy Mater. Sol. Cells*, vol. 220, no. October 2020, p. 110837, 2021, doi: 10.1016/j.solmat.2020.110837.

[24] B. R. Sutherland *et al.*, "Perovskite thin films via atomic layer deposition," *Adv. Mater.*, vol. 27, no. 1, pp. 53–58, 2015, doi: 10.1002/adma.201403965.

[25] G. Popov *et al.*, "Atomic Layer Deposition of PbI 2 Thin Films," *Chem. Mater.*, vol. 31, no. 3, pp. 1101–1109, 2019, doi: 10.1021/acs.chemmater.8b04969.

[26] J. Harjuoja, M. Putkonen, and L. Niinistö, "Exploiting volatile lead compounds as precursors for the atomic layer deposition of lead dioxide thin films," *Thin Solid Films*, vol. 497, no. 1–2, pp. 77–82, 2006, doi: 10.1016/j.tsf.2005.09.188.

[27] V. V Krisyuk, I. A. Baidina, and I. K. Igumenov, "ON THE CRYSTAL STRUCTURE AND SOME STRUCTURE- DEPENDENT PROPERTIES OF LEAD (ll) ß - D I K E T O N A T E S C ^ imF ^ Pb " CeF „" no. ll, pp. 199–206.

[28] N. P. Dasgupta *et al.*, "Atomic layer deposition of lead sulfide quantum dots on nanowire surfaces," *Nano Lett.*, vol. 11, no. 3, pp. 934–940, 2011, doi: 10.1021/nl103001h.

[29] F. Grillo, H. Van Bui, J. A. Moulijn, M. T. Kreutzer, and J. R. Van Ommen, "Understanding and Controlling the Aggregative Growth of Platinum Nanoparticles in Atomic Layer Deposition: An Avenue to Size Selection," *J. Phys. Chem. Lett.*, vol. 8, no. 5, pp. 975–983, 2017, doi: 10.1021/acs.jpclett.6b02978.

[30] F. Grillo, D. La Zara, P. Mulder, M. T. Kreutzer, and J. Ruud Van Ommen, "Oriented Attachment and Nanorod Formation in Atomic Layer Deposition of TiO2 on Graphene Nanoplatelets," *J. Phys. Chem. C*, vol. 122, no. 34, pp. 19981–19991, 2018, doi: 10.1021/acs.jpcc.8b05572.

[31] N. A. Strnad, B. M. Hanrahan, D. M. Potrepka, J. S. Pulskamp, R. J. Phaneuf, and R. G.

Polcawich, “Growth of thin film ferroelectric PZT, PHT, and antiferroelectric PHO from atomic layer deposition precursors,” *J. Am. Ceram. Soc.*, vol. 104, no. 3, pp. 1216–1228, 2021, doi: 10.1111/jace.17521.

[32] Y. Zhao *et al.*, “Tuning the reactivity of PbI2 film via monolayer Ti3C2Tx MXene for two-step-processed CH3NH3PbI3 solar cells,” *Chem. Eng. J.*, vol. 417, no. November 2020, p. 127912, 2021, doi: 10.1016/j.cej.2020.127912.

[33] D. Acuña, B. Krishnan, S. Shaji, S. Sepúlveda, and J. L. Menchaca, “Growth and properties of lead iodide thin films by spin coating,” *Bull. Mater. Sci.*, vol. 39, no. 6, pp. 1453–1460, 2016, doi: 10.1007/s12034-016-1282-z.

[34] R. Frisenda *et al.*, “Characterization of highly crystalline lead iodide nanosheets prepared by room-temperature solution processing,” *Nanotechnology*, vol. 28, no. 45, 2017, doi: 10.1088/1361-6528/aa8e5c.

[35] Q. Liang *et al.*, “Uniform, high crystalline, (100) crystal orientated perovskite films without PbI2 residue by controlling the nanostructure of PbI2,” *Org. Electron.*, vol. 53, no. June 2017, pp. 26–34, 2018, doi: 10.1016/j.orgel.2017.10.037.

[36] B. P. Dhamaniya *et al.*, “Orientation-Controlled (h0 l) PbI2Crystallites Using a Novel Pb-Precursor for Facile and Quick Sequential MAPbI3Perovskite Deposition,” *ACS Omega*, vol. 5, no. 48, pp. 31180–31191, 2020, doi: 10.1021/acsomega.0c04483.

[37] W. E. Morgan and J. R. Van Wazer, “Binding energy shifts in the X-ray photoelectron spectra of a series of related group IV-a compounds,” *J. Phys. Chem.*, vol. 77, no. 7, pp. 964–969, 1973, doi: 10.1021/j100626a023.

[38] V. I. Nefedov, “X-ray photoelectron spectra of halogens in coordination compounds,” *J. Electron Spectros. Relat. Phenomena*, vol. 12, no. 4, pp. 459–476, 1977, doi:

10.1016/0368-2048(77)85097-4.

[39] N. E. Richey, C. De Paula, and S. F. Bent, "Understanding chemical and physical mechanisms in atomic layer deposition," *J. Chem. Phys.*, vol. 152, no. 4, 2020, doi: 10.1063/1.5133390.

[40] Z. Zheng *et al.*, "In situ growth of epitaxial lead iodide films composed of hexagonal single crystals," *J. Mater. Chem.*, vol. 15, no. 42, pp. 4555–4559, 2005, doi: 10.1039/b510077a.

[41] P. A. Beckmann, "A review of polytypism in lead iodide," *Cryst. Res. Technol.*, vol. 45, no. 5, pp. 455–460, 2010, doi: 10.1002/crat.201000066.

[42] E. Klein, R. Lesyuk, and C. Klinke, "Insights into the formation mechanism of two-dimensional lead halide nanostructures," *Nanoscale*, vol. 10, no. 9, pp. 4442–4451, 2018, doi: 10.1039/c7nr09564c.

[43] A. Alberti, C. Bongiorno, E. Smecca, I. Deretzis, A. La Magna, and C. Spinella, "Pb clustering and PbI2 nanofragmentation during methylammonium lead iodide perovskite degradation," *Nat. Commun.*, vol. 10, no. 1, 2019, doi: 10.1038/s41467-019-09909-0.

SUPPLEMENTARY INFORMATION

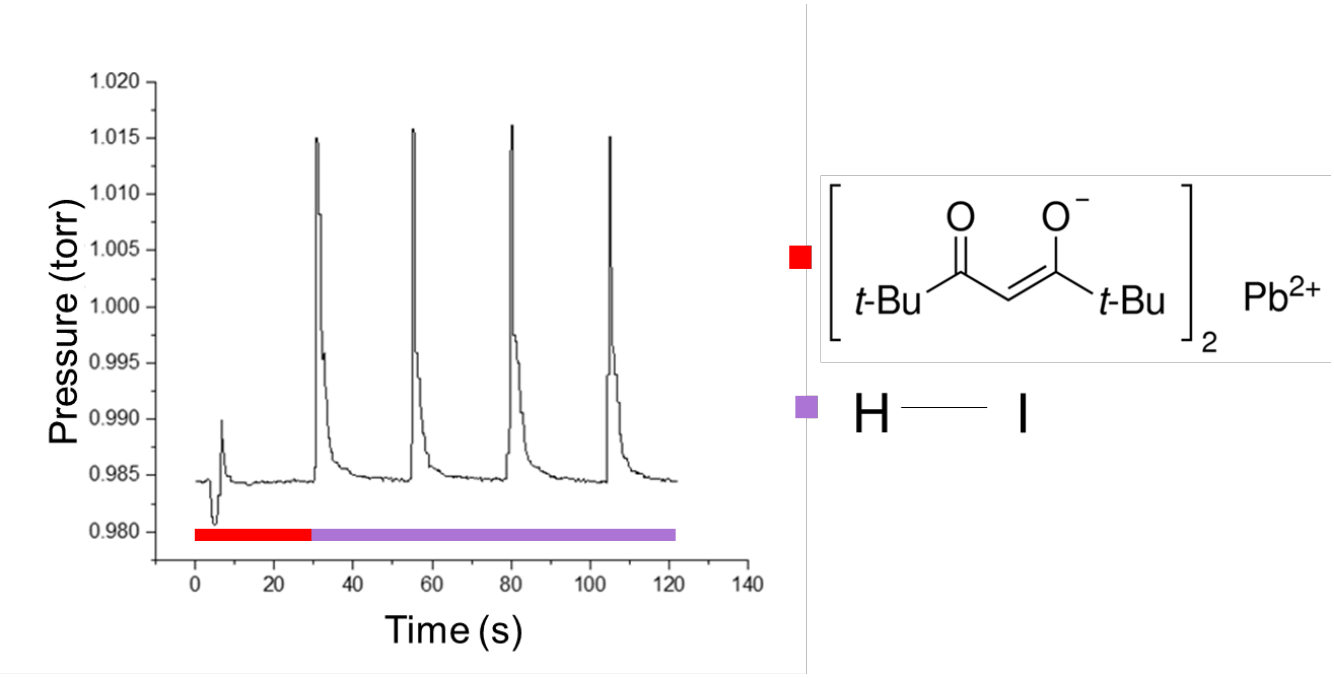

Figure S1. One cycle of PbI_2 by ALD. First, lead is dosed from a stainless-steel bubbler, followed by four sequential iodine doses. Purge times were 20 seconds between each precursor

dose.

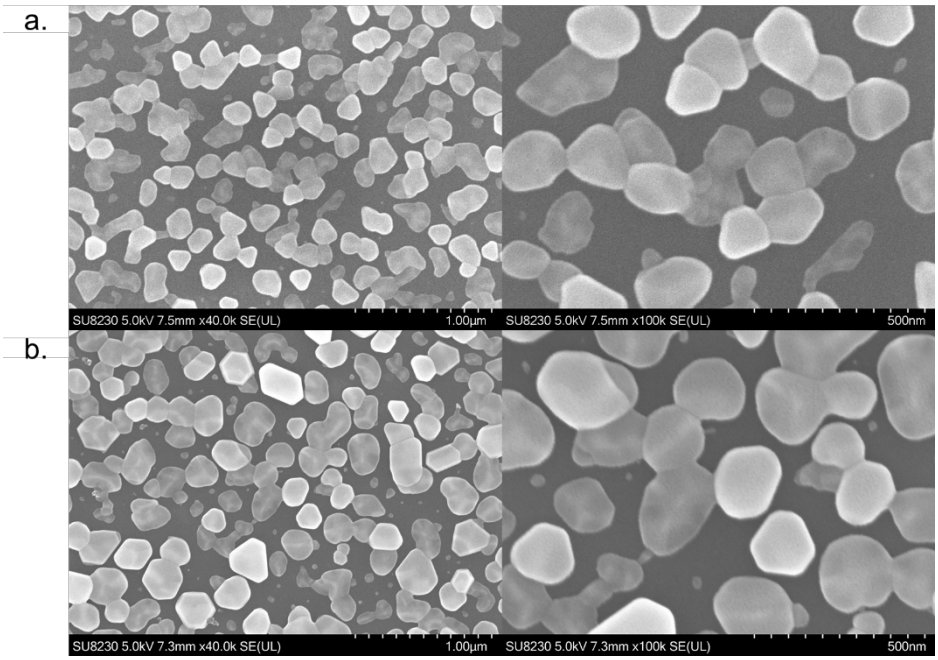

Figure S3. SEM of (a) 81 cycles and (b) 162 cycles of PbI_2 deposited on a silicon wafer at 120°C.

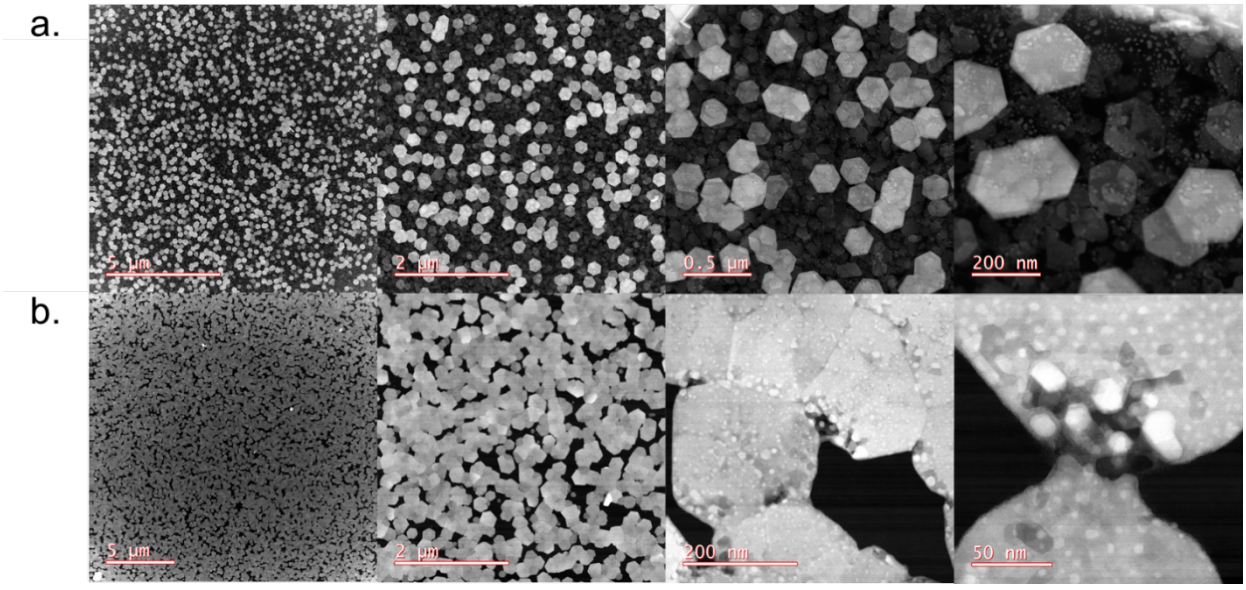

Figure S4. TEM Z-contrast images for PbI_2 deposited at 120°C after (a) 81 cycles and (b) 162 cycles.

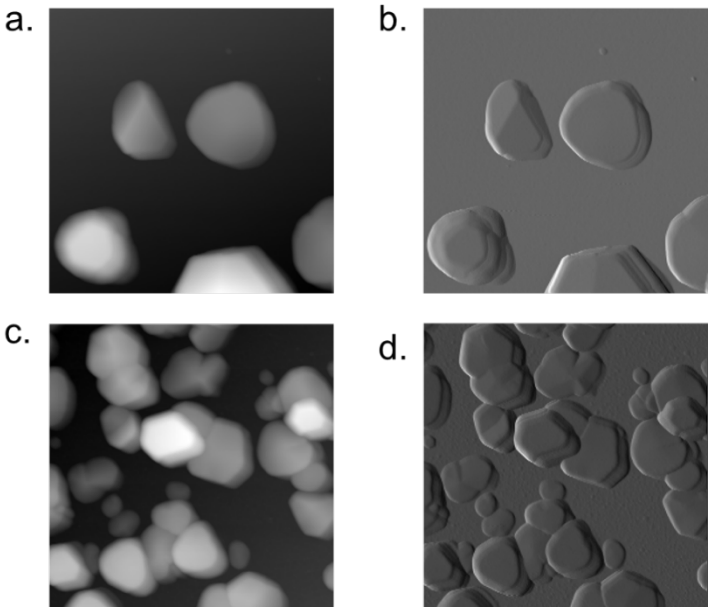

Figure S5. AFM images of PbI_2 by ALD on silicon wafers at 120°C where (a) and (b) are zsensor and amplitude error plots for 81 cycles, respectively, and (c) and (d) are zsensor and amplitude error plots for 162 cycles, respectively.